First-principles investigation on redox properties of *M*-doped CeO_2 (*M*=Mn,Pr,Sn,Zr)

Yuanhao Tang,[1,2] Hua Zhang,[1] Lixia Cui,[1] Chuying Ouyang,[3] Siqi Shi,[1,2,*] Weihua Tang,[1] Hong Li,[2] Jong-Sook Lee,[4] and Liquan Chen[2,4]

[1]*Department of Physics, Center for Optoelectronics Materials and Devices, Zhejiang Sci-Tech University, Xiasha College Park, Hangzhou 310018, China*

[2]*Renewable Energy Laboratory, Institute of Physics, Chinese Academy of Sciences, Beijing 100190, China*

[3]*Department of Physics, Jiangxi Normal University, Nanchang 330022, China*

[4]*School of Materials Science and Engineering, Chonnam National University, Gwangju 500-757, Republic of Korea*

(Received 5 June 2010; published 3 September 2010)

The effects of *M* (*M*=Mn,Pr,Sn,Zr) doping on the redox thermodynamics of CeO_2 have been investigated using first-principles density-functional theory calculations with the on-site Coulomb interaction taken into account. Two different mechanisms for the O-vacancy formation in doped CeO_2 have been clarified. Compared with the case of pure CeO_2, the decrease in the O-vacancy formation energy for the Zr-doped CeO_2 is mostly caused by the structural distortion, whereas the decrease for Mn-, Pr-, or Sn-doped CeO_2 originates from the electronic modification as well as from the structural distortion. It is found that the electronic modification occurs in those dopants whose uttermost atomic orbitals are half or fully occupied by the filling of the excess electrons left by the formation of the O vacancy. Two effects also contribute to concentration dependence of the O-vacancy formation energies for different dopant species.

DOI: 10.1103/PhysRevB.82.125104 PACS number(s): 82.45.Gj, 82.60.Lf, 61.72.jd, 71.15.Mb

I. INTRODUCTION

Cerium oxide based materials are important catalysts for many technological applications such as automotive three-way catalysts[1–3] for simultaneous conversion of nitrogen oxides (NO_x), carbon monoxide (CO) and hydrocarbons, and catalysts for the hydrogen production by fuel reforming.[4,5] The successful applications of CeO_2 as catalysts are related to the facile redox cycling between trivalent and tetravalent Ce ions and the high mobility of bulk oxygen species which allows ceria to behave as an oxygen buffer. The latter quality makes CeO_2 promising electrolyte material for intermediate temperature solid oxide fuel cells.[6–8]

Pure CeO_2 itself is not a good ionic conductor due to the lower oxygen ion vacancy concentration and the higher electronic conductivity under reducing conditions.[9] However, a significant increase in ionic conductivity can be achieved by doping which generates the O vacancies.[10] In addition, the reduction in CeO_2 is controlled by the nature of the reduction mechanism.[11,12] Therefore, a comprehensive understand on the O-vacancy formation and redox mechanisms of the doped CeO_2 will be valuable.

Many experimental studies concerning the improvement of redox properties of CeO_2 at high temperatures have been carried out. Sun *et al.*[13,14] reported the particle size and microstructure can have significant influences on catalytic activity. Xiao *et al.*[15] prepared nanostructured $Ce_{0.9}Sm_{0.1}O_{1.95}$ and found this material shows enhanced activity for oxygen reduction. Very recently, Gao *et al.*[16] showed the direct atomic-scale observation of an electrically driven redox process in cerium oxide films. On the other hand, there have been some theoretical studies on fundamental properties of CeO_2. Skorodumova *et al.*[17] and Andersson *et al.*[18] described structural, thermodynamic, and electronic properties of cerium oxide and found that the on-site Coulomb interaction *U* has a significant influence on the calculated results. Da Silva[19] explained the effect of the volume expansion on the reduction in CeO_2. Shi *et al.*[20,21] calculated the bonding, optical, lattice dynamical, and surface properties of ceria.

Previous experimental and theoretical investigations suggest that the redox properties of ceria can be enhanced by one or more dopants.[22–24] Doping with Zr (Ref. 25) or Pd (Ref. 26) can increase the oxygen storage capacity. Doping with reducible elements such as Pr and Sn enhances the low-temperature reducibility.[27–29] Oxide ion conductivity can be improved by doping with trivalent ions such as Sc, Y, La, Nd, Sm, Gd, Dy, and Lu due to the introduction of oxygen vacancies.[24] Liang *et al.*[30] reported that due to the small radius, Mn^{x+} ions can enter into the ceria lattice to form solid solutions, increasing the amount of oxygen vacancies and thus enhancing the catalytic activities. Very recently, Xiao *et al.*[31] prepared Y, La, Zr, Pr, and Sn doped ceria with a flowerlike structure and found that Pr- or Sn-doped ceria exhibits an excellent catalytic reactivity on CO oxidation reaction.

As for the effects of the dopant on redox properties of CeO_2, there have been some systematical investigations. A common opinion is that, compared to pure CeO_2, reduction is facilitated and the reducibility increases with the decrease in the ionic radius of the dopant associated with the structural distortion as discussed in Ref. 22. On the other hand, Ref. 22 also mentioned that the rule seems not to apply to the Pb-doping case. This makes us conjecture whether there exists the factor favorable for the O-vacancy formation other than the structural distortion, which can in turn explain the Pb-doping case. In addition, it is also of great importance to make comparison among various doped CeO_2 systems so as to clarify the effects of dopant species from the standpoint of materials design. In the current paper, we apply first-principles calculations with on-site Coulomb interaction in CeO_2 doped with Mn, Pr, Sn, or Zr. The effect of the doping on the O-vacancy formation is investigated. The electron redistribution mechanism during the process of the O-vacancy

formation is examined. We also study the influence of the dopant concentration on the redox properties of CeO_2.

II. COMPUTATIONAL DETAILS

The calculations are performed using the Vienna *ab initio* simulation package (VASP) in the framework of the projector augmented wave method.[32–34] The Perdew-Burke-Ernzerhof (PBE) functional is used for the exchange correlation.[35] The density-functional theory (DFT) method has been shown suitable to describe the CeO_2.[17,36,37] Furthermore, in order to account for the strong on-site Coulomb repulsion among the Ce $4f$ electrons, a Hubbard parameter U is added to the DFT functional (DFT+U). As previously discussed,[18,38,39] U value can significantly influence the calculated results for CeO_2 and $CeO_{2-\delta}$. Here, we choose a U value of 4.5 eV as suggested by Fabris *et al.*[40] Note that the same U value is used for the description of the strong on-site Coulomb repulsion among Pr $4f$ and Mn $3d$ electrons, which is shown to be reasonable by fitting to the experimentally available parameters of PrO_2 and MnO such as lattice constants and band gap. The value removes the self-interaction error and thus improves the description of the correlation effects.

The configurations of Ce $5s^25p^66s^25d^14f^1$, O $2s^22p^4$, Mn $3d^64s^1$, Pr $5s^25p^66s^25d^14f^2$, Sn $5s^25p^2$, and Zr $4d^35s^1$ are treated as the valence electrons. In order to avoid the interaction between the two images of the displaced atom due to the periodic boundary condition, we model defect properties using a $2\times2\times2$ supercell with 96 sites, derived from the ideal fluorite structure. For small solute concentrations, the volume of the supercell is set equal to the calculated volume of pure ceria.[18] We use a plane-wave cut-off energy of 400 eV and $2\times2\times2$ Monkhorst-Pack k-point mesh[41] with Gaussian smearing of 0.20 eV (Ref. 42) for the defect properties. For a more accurate calculation of the electronic density of states (DOS), we apply $4\times4\times4$ k-point mesh and the modified tetrahedron method.[43]

III. RESULTS AND DISCUSSION

A. O-vacancy formation energies in pure CeO_2 and $Ce_{1-x}M_xO_2$ ($x=0.0312$)

Pure bulk CeO_2 has the fluorite structure in which the cations have an expanded face-centered-cubic arrangement with all tetrahedral holes filled by the anions as shown in Fig. 1(a). It is well known that the oxygen storage capacity of CeO_2 is closely correlated with the formation and migration of the O vacancies in CeO_2. We calculate the O-vacancy formation energy (E_{vac}) by

$$E_{vac} = E(cell_{vac}) + \frac{1}{2}E(O_2) - E(cell),$$

where $E(cell_{vac})$ and $E(cell)$ are the total energies of the optimized supercells with and without an O vacancy, and $E(O_2)$ is the total energy for the ground state of an optimized oxygen molecule in the gas phase. Note that, during the process of the O-vacancy formation, the released O atom is supposed to form oxygen molecule.

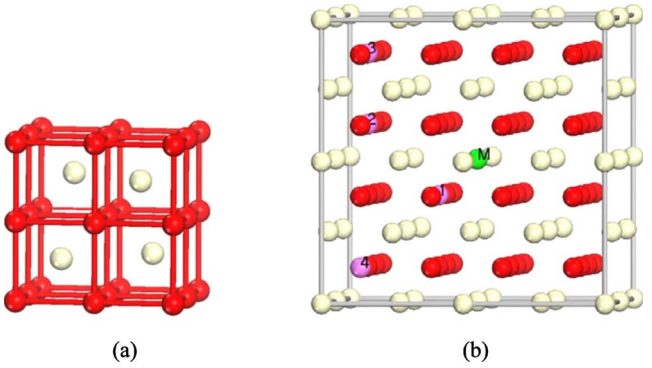

FIG. 1. (Color online) The ideal fluorite structure of CeO_2 and the supercell used for the defect properties. (a) A unit cell of CeO_2 centered at the cubic oxygen sublattice. (b) The $2\times2\times2$ supercell of M (M=Mn,Pr,Sn,Zr) doped CeO_2. The numbers 1–4 indicate the possible positions of the O vacancy in the system, respectively. White, red, green, and pink spheres represent the Ce, O, M, and O vacancy, respectively.

The calculated E_{vac} value for the bulk CeO_2 is 3.10 eV which is very close to that (3.03 V) of Yang *et al.*[25] using the same PBE+U formulation with the U value of 6.0 eV. Andersson *et al.*[18] obtained the O-vacancy energy of 3.61 eV from the local-density approximation plus U calculations with U=6.0 eV. The calculated values are underestimated by 1.6 eV compared with the experimental value of 4.72 eV reported by Panhans *et al.*[44] This underestimation is largely contributed by the overestimation of the O_2 molecule formation energy.[18,22] The overestimation of the formation energy of O_2 is a common feature in the DFT calculations.

When an O vacancy is formed, two electrons left behind will condense into localized $4f$ level traps from the two nearest-neighboring (NN) Ce ions, thus transforming Ce^{4+} into Ce^{3+} (Ref. 45) and leading to a nonsymmetrical relaxation pattern.[18,25,26] However, this cannot be obtained from the ideal fluorite CeO_2. Actually, when the relaxation begins from the perfect structure, all the ions surrounding the O-vacancy still maintain the symmetry and the excess electrons are found being equally localized on the four NN Ce ions. This phenomenon has also been observed by Jiang *et al.*[46] In order to get the energetically favorable structure, the system has to be distorted by moving the neighboring O^{2-} ions away from their original fluorite lattice positions. Indeed, the total energy for the distorted configuration is 0.46 eV lower than that for the perfect fluorite lattice structure. Figure 2(a) shows the displacements of the ions around the O vacancy in $CeO_{2-\delta}$ with δ=0.0312. All four nearest-neighboring cations move away from the O vacancy with two Ce^{3+} ions by 0.15 Å and other two Ce^{4+} ions by 0.176 Å, respectively. The neighboring O ions move outward by 0.123–0.289 Å, except that one O ion, which is a nearest neighbor to the two reduced cations, moves inward by 0.016 Å.

As we have mentioned before, the redox process of CeO_2 is influenced by the presence of dopant. Figure 1(b) shows the possible O-vacancy configurations derived from the $2\times2\times2$ supercell with one Ce replaced by M^{4+} ion with M being Mn, Pr, Sn, or Zr. The O-vacancy formation energies

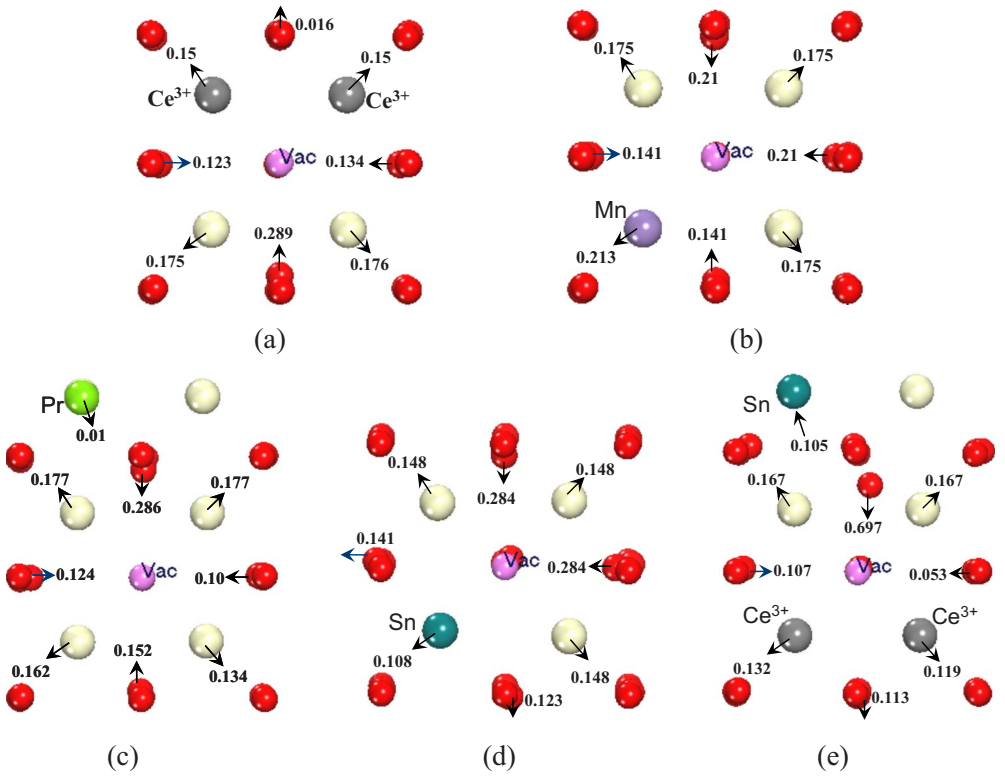

FIG. 2. (Color online) Displacement patterns of the ions around the O vacancy for the (a) pure and [(b)–(e)] M-doped system (M =Mn,Pr,Sn). In (a), (b), (d) and (c), (e), the dopant ions are the first and second nearest neighbors to the O vacancy, respectively. White, gray, red, pink, pansy, green, and dark green sphere represent the Ce^{4+}, Ce^{3+}, O, O vacancy, Mn, Pr, and Sn, respectively. For the distinct purpose, the positions of Ce^{3+}, O vacancy and doped element M are also labeled with the corresponding symbols.

for the M-doped CeO_2 systems are summarized in Fig. 3. The notations of 1NN to 4NN are for the O vacancies at the first, second, third, and fourth nearest neighbors to the doped ions, respectively. It can be seen that all these dopants significantly lower the O-vacancy formation energies of CeO_2, indicating the possibility of increasing the oxygen storage capacity by doping. It is interesting that Mn-doped CeO_2 has the lowest O-vacancy formation energy with a value of −0.434 eV for the 1NN configuration which may imply a spontaneous creation of O vacancy in Mn-doped CeO_2. The configuration with the location of the O vacancy at the 1NN site is the most stable for Mn- and Zr-doped CeO_2, whereas Pr-doped CeO_2 has the lowest O-vacancy formation energy for the 2NN configuration. On the other hand, the O-vacancy formation energy in Sn-doped CeO_2 is very close for all configuration of 1NN to 4NN. The differences in O-vacancy formation energy between these dopants should be ascribed to the electronic structure of the solid solutions as discussed below.

B. Atomic and electronic structures in M-doped CeO_2

1. Mn-doped CeO_2

According to Fig. 3, the O-vacancy formation energy in $Ce_{1-x}M_xO_2$ (x=0.0312) is the lowest for M=Mn among the dopants of the current investigation and even negative for the 1NN configuration. The facileness of the O-vacancy formation in $Ce_{1-x}Mn_xO_2$ (x=0.0312) may be attributed to the small size (0.52 Å) of Mn^{4+}. This is consistent with the suggestion by Andersson *et al.*[22,23,47] that there should be a strong dependence of the O-vacancy formation energy on the ionic radius of the dopants. Figure 2(b) shows the displacement pattern in $Ce_{1-x}Mn_xO_{2-\delta}$ ($x=\delta$=0.0312) with the O-vacancy 1NN to Mn ion. It can be seen that all the nearest-neighboring cations move away from the O vacancy with three Ce ions by 0.175 Å and one Mn ion by 0.213 Å, respectively. The neighboring O ions move inward by 0.141–0.21 Å. Therefore, compared with the case of $CeO_{2-\delta}$

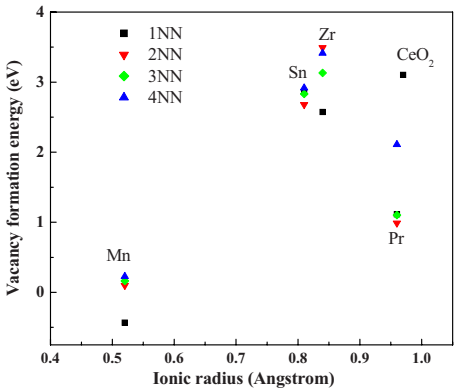

FIG. 3. (Color online) The O-vacancy formation energy in pure CeO_2 and M-doped CeO_2 (M=Mn,Pr,Sn,Zr). The notations of 1NN to 4NN indicate that the O vacancies are the first, second, third, and fourth nearest neighbors to the dopant ions, respectively.

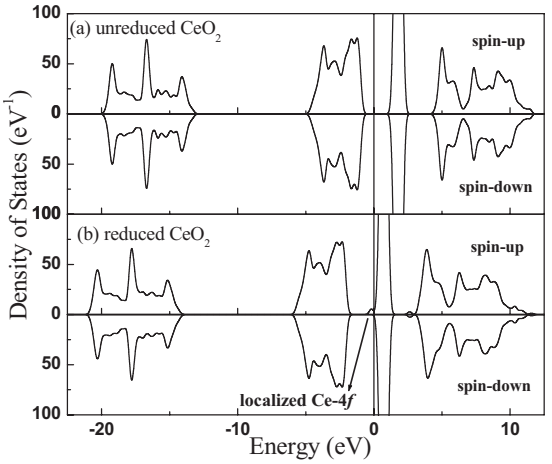

FIG. 4. TDOS for (a) unreduced CeO_2 and (b) reduced CeO_2. The upper and lower panels represent the spin-up and spin-down channels, respectively. The zero point of the energy axis corresponds to the Fermi level.

(δ=0.0312), the ions in the neighborhood of the O vacancy are more perturbed, and thus significantly enlarge the octahedral interstitial positions to be favorable for O-vacancy formation.

Figure 4 shows the total DOS (TDOS) for the pure CeO_2 without and with an O vacancy. It is found that CeO_2 is an insulator and the valence band is mostly contributed by O 2*p* and some contributions by Ce 5*d* and Ce 4*f*, whereas the narrow empty band which is situated above the Fermi level is the Ce 4*f*. The respective energy gaps between the O 2*p* valance-band top and the unoccupied Ce 4*f* and Ce 5*d* band bottom are 2.23 eV and 5.34 eV, respectively, which are in good agreement with the experimental values (3.0 and 6.0 eV).[48] Once CeO_2 is reduced by removing an O atom, a new peak emerges between O 2*p* valance-band top and unoccupied Ce 4*f* band bottom which is regarded as the localized Ce 4*f*.[45,49,50] The localized Ce 4*f* states are assigned to the two Ce^{3+} ions surrounding the O vacancy as discussed

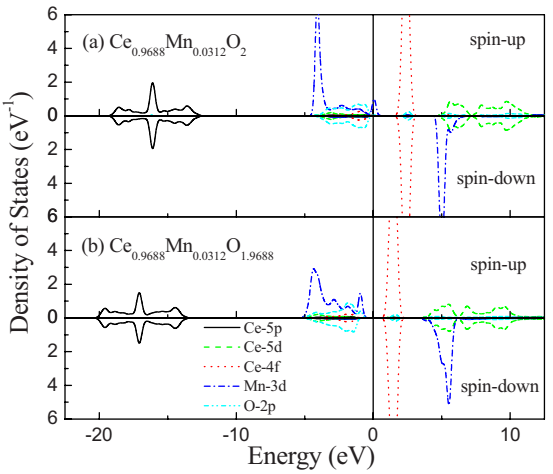

FIG. 5. (Color online) PDOS for (a) unreduced and (b) reduced $Ce_{1-x}Mn_xO_2$ (x=0.0312). The upper and lower panels represent the spin-up and spin-down channels, respectively. The zero point of the energy axis corresponds to the Fermi level.

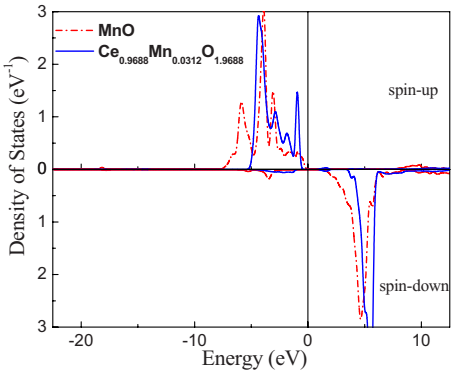

FIG. 6. (Color online) PDOS of Mn 3*d* for cubic MnO and $Ce_{1-x}Mn_xO_{2-\delta}$ ($x=\delta$=0.0312). The zero point of the energy axis corresponds to the Fermi level. The upper and lower panels represent the spin-up and spin-down channels, respectively.

above. Namely, the two electrons left upon the formation of the O vacancy in pure CeO_2 localize on the two NN Ce ions.

Figure 5 shows the partial DOS (PDOS) for the unreduced and reduced $Ce_{1-x}Mn_xO_2$ (x=0.0312). There are some gap states between the O 2*p* valence-band top and the unoccupied Ce 4*f* band bottom compared with the case of pure CeO_2. Further analysis indicates that these gap states are mainly contributed by Mn^{4+} 3*d* electrons. The half-occupied gap states in $Ce_{1-x}Mn_xO_{2-\delta}$ ($x=\delta$=0.0312) become filled mainly by the localization of the electrons left at the Mn 3*d* states. In other words, the formation of the O vacancy in $Ce_{1-x}Mn_xO_2$ (x=0.0312) causes the two excess electrons to preferentially occupy Mn 3*d* states, resulting in the reduction in $Mn(IV) \Rightarrow Mn(II)$ instead of the usual reaction $Ce(IV) \Rightarrow Ce(III)$ in pure CeO_2. The PDOS of Mn 3*d* states in $Ce_{1-x}Mn_xO_{2-\delta}$ ($x=\delta$=0.0312) and cubic MnO, shown in Fig. 6, indicate only small difference between the electronic structures of the two systems with different chemical environments.

To further understand the mechanism of the electron transfer associated with the formation of the O vacancy, we plot the integrated spin as a function of sphere radius around Mn for δ=0 and δ=0.0312 in $Ce_{1-x}Mn_xO_{2-\delta}$ as shown in Fig. 7. It can be clearly seen that values of net spin of 2.97 and 4.5 electrons at integration radii of 0.67 Å and 1.10 Å correspond to Mn^{4+} and Mn^{2+} ions, respectively. These fea-

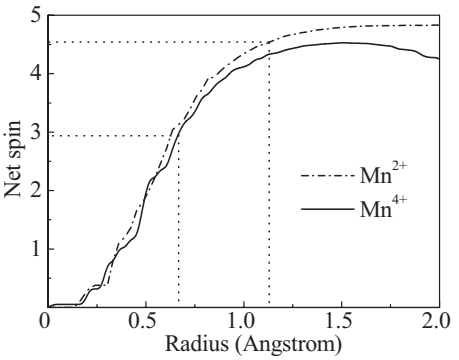

FIG. 7. Integrated spin of Mn atom for unreduced (solid line) and reduced (dashed line) $Ce_{1-x}Mn_xO_2$ (x=0.0312).

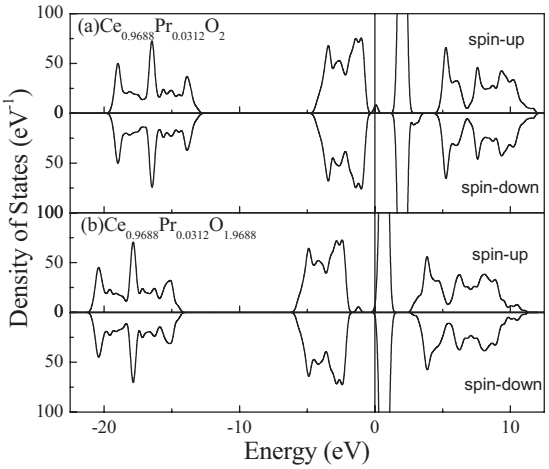

FIG. 8. TDOS for (a) unreduced and (b) reduced $Ce_{1-x}Pr_xO_2$ ($x=0.0312$). The zero point of the energy axis corresponds to the Fermi level. The upper and lower panels represent the spin-up and spin-down channels, respectively.

tures indeed imply that for $Ce_{1-x}Mn_xO_2$, the initial reduction occurs on $Mn(IV) \Rightarrow Mn(II)$.

Experimental results appear to support the conclusion of the present investigation. Shan *et al.*[51] investigated the MnO_x-CeO_2 system using x-ray powder diffraction and temperature programmed reduction indicating that the reduction in Mn ion in MnO_x-CeO_2 system leads to the high catalytic activity for the soot oxidation. Kang *et al.*[52] suggested that Mn^{2+}, not Mn^{3+}, should be incorporated due to the size compatibility with Ce^{4+}. Therefore, it can be concluded that not only the significant structural distortions but also the electronic modification causes the reduction in the O-vacancy formation energy, contributing to a high catalytic activity.

2. *Pr-doped* CeO_2

Figure 2(c) shows the relaxed structure of $Ce_{1-x}Pr_xO_{2-\delta}$ ($x=\delta=0.0312$) with an O vacancy located at the 2NN to the doped Pr ion. Four NN Ce ions move outward from 0.134 to 1.777 Å whereas the Pr ions almost keep unchanged. The nearest-neighboring O ions move inward in the range from 0.10 to 0.286 Å. The O-vacancy-induced structural distortion is smaller for the Pr-doped CeO_2 than for the Mn-doped system, which is represented by the higher O-vacancy formation energy in the Pr-doped CeO_2 than that in the Mn-doped CeO_2.

It should be noted that the O-vacancy formation energy for the Pr-doped CeO_2 is about one third of that for the pure CeO_2 despite similar sizes. This can be explained by the electronic structure. The analysis of the TDOS reveals that a new peak corresponding to metal-induced gap states (MIGSs) is observed between the unoccupied Ce $4f$ band bottom and O $2p$ valance-band top in $Ce_{1-x}Pr_xO_2$ ($x=0.0312$) as shown in Fig. 8(a), which is similar to that in $Ce_{1-x}Mn_xO_2$ ($x=0.0312$). It is also seen from Fig. 8(b) that the MIGS for $Ce_{1-x}Pr_xO_{2-\delta}$ ($x=\delta=0.0312$) move away from the Fermi level. The PDOS-based analysis indicates that the MIGS are mainly composed by the Pr $4f$ states. This suggests that the electrons left upon the formation of the O vacancy may transfer to the Pr^{4+} ion instead of the Ce^{4+} ion, although the Pr ion is the second nearest neighbor to the O vacancy. Similar conclusion was drawn from the investigation of the O vacancy on CeO_2 (111) surface by Ganduglia-Pirovano *et al.*[53] and Li *et al.*[54] They found that the excess electrons do not localize on the nearest-neighbor Ce ions to the O vacancy but on the second-nearest-neighbor Ce ions.

The calculated Pr $4f$ states occupancy of 1.44 electrons in $Ce_{0.9688}Pr_{0.0312}O_2$ is consistent with that of 1.5–1.6 electrons in PrO_2 by Kotani and co-workers.[55–57] In contrast, the calculated occupancy of Pr $4f$ states in $Ce_{1-x}Pr_xO_{2-\delta}$ ($x=\delta=0.0312$) is 1.96 electrons, which suggests that the formation of the O-vacancy results in the transformation of the Pr^{4+} ion to Pr^{3+} ion. Our calculation results agree well with the x-ray photoemission spectroscopy observation by Xiao *et al.*,[31] which indicates that there exist the variable valence states of Pr ions in Pr-doped CeO_2. Tran *et al.*[58] reported that there is Jahn-Teller distortion in PrO_2 which may explain the structural distortions around the O vacancy. Therefore, we believe that it is the variable valence states of Pr ions and Jahn-Teller distortion in PrO_2 that cause the much smaller O-vacancy formation energy in $Ce_{1-x}Pr_xO_{2-\delta}$ ($x=\delta=0.0312$) compared with that in pure CeO_2.

3. *Sn-doped* CeO_2

As is shown in Fig. 3, the formation energies of the O vacancy located at the 1NN, 2NN, 3NN, and 4NN to the Sn ion for the Sn-doped CeO_2 are very close to each other. This would suggest that the O vacancy can be randomly distributed in the CeO_2 lattice. However, the details in the lattice distortions and the charge transfer associated with the formation of the O vacancy are found quite different depending on the dopant-vacancy locations.

Figures 2(d) and 2(e) show the respective relaxed structures for $M=Sn$ in $Ce_{1-x}M_xO_{2-\delta}$ ($x=\delta=0.0312$) with an O vacancy located at the 1NN and 2NN to the Sn ion. For the former, three Ce and one Sn ions neighboring to the O vacancy move outward by 0.148 Å and 0.108 Å, respectively. Two of the nearest-neighboring O ions move inward by 0.284 Å with the other O ions outward by 0.123 Å. However, for the latter, four neighboring Ce ions move outward by 0.119–0.167 Å and the neighboring O ions move by about 0.107–0.697 Å. Obviously, the cations around the O vacancy in $Ce_{1-x}M_xO_{2-\delta}$ ($x=\delta=0.0312$) for $M=Mn$ and Pr are more drastically distorted than those for $M=Sn$.

Since Sn doping has such a large effect on the O-vacancy formation energy and atomic structure of CeO_2 as discussed above, it is essential to understand the electronic structure of Sn-doped CeO_2. The analysis of the TDOS for $Ce_{1-x}Sn_xO_2$ ($x=0.0312$) indicates that the valence band mostly exhibits O $2p$ character with some contribution from Ce $4f$ and Ce $5d$ states, and there are Sn-induced electronic states below the O $2p$ band as shown in Fig. 9(a). The respective energy gaps between the O $2p$ valance-band top and the unoccupied Ce $4f$ and Ce $5d$ band bottom are about 1.94 and 5.24 eV, which are slightly smaller than those for pure CeO_2. Once an O vacancy is formed at the 2NN to the Sn ion, a new peak emerges between the O $2p$ and Ce $4f$ gap state as clearly shown in Fig. 9(b). To a large extent, this new peak in

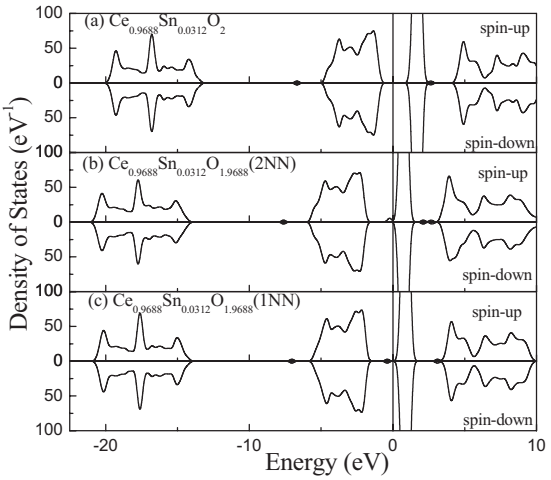

FIG. 9. TDOS for (a) $Ce_{1-x}Sn_xO_2$ (x=0.0312), (b) $Ce_{1-x}Sn_xO_{2-\delta}$ ($x=\delta$=0.0312) with the O-vacancy 2NN to the Sn ions, and (c) $Ce_{1-x}Sn_xO_{2-\delta}$ ($x=\delta$=0.0312) with the O-vacancy 1NN to the Sn ions. The zero point of the energy axis corresponds to the Fermi level. The upper and lower panels represent the spin-up and spin-down channels, respectively.

$Ce_{1-x}Sn_xO_{2-\delta}$ ($x=\delta$=0.0312) is similar to that in $CeO_{2-\delta}$ (δ=0.0312) which is considered to be the localized Ce 4f states [see Fig. 4(b)]. On the contrary, for the case of the O vacancy at the 1NN to the Sn ion, there is a symmetrical peak below the Fermi level as shown in Fig. 9(c).

In order to get further insight into the difference between Figs. 9(b) and 9(c), we plot the PDOS of Sn and Ce atoms nearest neighboring to the O vacancy in $Ce_{1-x}Sn_xO_{2-\delta}$ ($x=\delta$=0.0312) as shown in Fig. 10. It can be seen from Fig. 10(b) that upon the formation of an O vacancy at the 2NN to the Sn^{4+} ion, there exists a new localized Ce 4f state and a transfer of 1.70 electrons to two neighboring Ce ions is observed, which is typical of the reduction in the Ce^{4+} ion.

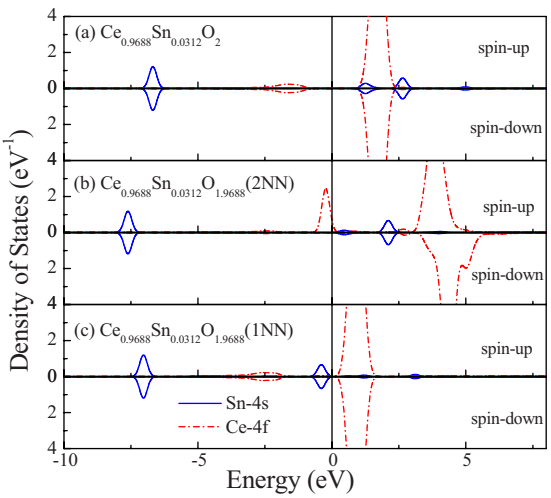

FIG. 10. (Color online) Ce 4f and Sn 4s PDOS corresponding to Fig. 9: for (a) $Ce_{1-x}Sn_xO_2$ (x=0.0312), (b) $Ce_{1-x}Sn_xO_{2-\delta}$ ($x=\delta$=0.0312) with the O-vacancy 2NN to the Sn ions, and (c) $Ce_{1-x}Sn_xO_{2-\delta}$ ($x=\delta$=0.0312) with the O-vacancy 1NN to the Sn ions. The zero point of the energy axis corresponds to the Fermi level.

However, the Sn 4s state in Fig. 10(c) is completely occupied which is characteristic of the transfer of excess electrons to the Sn ion so that the reduction occurs on Sn^{4+} for O vacancy at the 1NN to Sn ion. A competition between these two reduction mechanisms is reflected in the fact that the O-vacancy formation energies are almost the same for the two cases.

4. *Zr-doped* CeO_2

It has been found that the redox properties and thermal stability of CeO_2 are greatly enhanced by doping with ZrO_2. Thus the properties of $Ce_{1-x}Zr_xO_{2-\delta}$ have been extensively investigated experimentally.[59–62] Moreover, there are also a number of theoretical studies reported previously in the literatures.[25,63–65] Using the DFT+U calculations, we reproduce the previous conclusion. We obtain the O-vacancy formation energy in $Ce_{1-x}Zr_xO_{2-\delta}$ ($x=\delta$=0.0312) as 2.57 eV for the 1NN configuration, which is consistent with 2.38 eV reported by Yang *et al.*[25] The O vacancy is most easily formed at the 1NN to Zr ion and the electrons left by the released oxygen localize on the two Ce ions neighboring to the vacancy as in the case of pure CeO_2. Structural distortion induced by Zr dopant is supposed to be the main mechanism for the decrease in O-vacancy formation energy.

5. *Summary of the dopant effects*

Based on the above results and discussion, it is found that dissolving small amounts of MnO_2, PrO_2, SnO_2, and ZrO_2 can result in the decrease in the O-vacancy formation energy in CeO_2. There shall be two different reduction mechanisms upon the formation of the O-vacancy in doped CeO_2. When an O vacancy is formed in pure CeO_2 or Zr-, Si-, Ti-doped CeO_2,[22,23,45] the excess electrons localize on two NN Ce ions as previously suggested, and the increased reducibility is largely due to the structural distortions. However, for the Mn-, Sn-, Pb-,[22] or Pr-doped CeO_2 system, the initial reduction may occur on the dopants instead of the Ce^{4+}, thus lowering the O-vacancy formation energy not only by structural distortion but also by the electronic modification. Note that the outermost orbital electronic configuration for nonrare-earth metal ions Mn^{2+}, Sn^{2+}, and Pb^{2+} are $3d^5$, $5s^2$, and $6s^2$, respectively, which are half or fully occupied and is significantly different from that of $4f^2$ for rare-earth metal ion Pr^{3+}. Here, we may assume that the electronic modification usually occurs on the dopant ion whose uttermost atomic orbital, due to the filling of the excess electrons left by the formation of the O vacancy, will be half or fully occupied. It is worth mentioning that Andersson *et al.*[22] dealt with the Pb-doped CeO_2 and also found that the initial reduction occurs by $Pb^{4+} \rightarrow Pb^{2+}$ instead of the usual $Ce^{4+} \rightarrow Ce^{3+}$, although the electronic modification contributing to the O-vacancy formation other than the structural distortion is not specifically proposed. As for the Pr-doped CeO_2, Pr is known to adopt the trivalent state much more easily than Ce so that the initial reduction also occur on the Pr^{4+} ion.[66] The same is true for the Tb-doped CeO_2, which has been experimentally revealed by Wang *et al.*[67] In fact, Ce, Tb, and Pr are the only rare-earth metals whose oxides commonly exist in both +3 and +4 oxidation states.

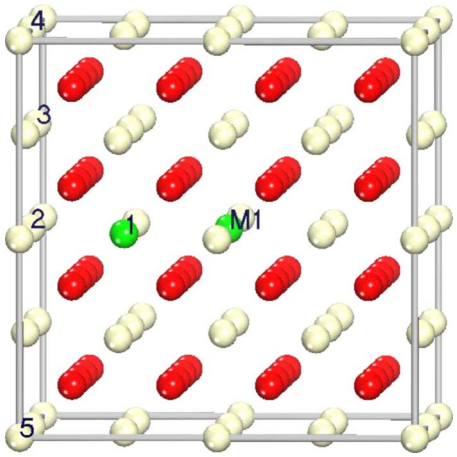

FIG. 11. (Color online) The $2\times2\times2$ supercell of fluorite structure $Ce_{1-x}M_xO_2$ ($x=0.0625$) with M=Mn Pr, Sn, or Zr. M_1 represents the first dopant ion located in the supercell center. The numbers 1–5 represent five possible cation sites by the second dopant ion M_2 in the Ce sublattice.

Mn in $Ce_{1-x}M_xO_{2-\delta}$ ($x=\delta=0.0312$) leads to the largest structural distortion of the ions around the O vacancy which is largely due to the smallest radius of Mn ion compared to those of Pr, Sn, and Zr dopants. The degree of the local atomic structure distortion for M=Pr is between those for Mn and Sn, although Pr ion has a larger radius than Sn ion. This can be ascribed to the Jahn-Teller effect in PrO_2 which causes larger perturbation of the local atomic structure. All these doped CeO_2 systems exhibit the larger structural distortion compared with pure CeO_2. Furthermore, the order of the size of the calculated O-vacancy formation energy is consistent with the displacements of the ions around the O vacancy.

C. Effect of dopant concentration (x) in $Ce_{1-x}M_xO_{2-\delta}$

In order to find the effects of dopant concentrations on the O-vacancy formation, we have studied $Ce_{1-x}M_xO_2$ system with M being Mn, Pr, Sn, or Zr and $x=0.0312$, 0.0625, or 0.09375. In Sec. III B, we have discussed the case of $x=0.0312$ using the $2\times2\times2$ supercell and the same $2\times2\times2$ supercells are modeled for $x=0.0625$ and 0.09375 in order to keep the same O-vacancy concentration.

For the construction of $Ce_{1-x}M_xO_2$, we place the first dopant ion (M_1) in the center of the $2\times2\times2$ supercell. Then, another dopant ion (M_2) is introduced into the supercell. In this way, there are five different sites around M_1 in the Ce sublattice which can be occupied by M_2 as shown in Fig. 11. Results show that when M_2 is the 1NN or 2NN to M_1, the system will be energetically favorable. Due to the similar total energies for these two structures, M_2 is assumed to occupy the 1NN site of M_1. Finally, an O vacancy is created. In the oxygen sublattice, there are four M_1-O distances and eight M_2-O distances. All the possible defect structures and O-vacancy formation energies are summarized in Table I. For M=Pr and Sn with $x=0.0625$ in $Ce_{1-x}M_xO_{2-\delta}$ ($\delta=0.0312$), the defect structures with an O vacancy located at the 1NN to M_1 and 1NN or 2NN to M_2 have the smallest O-vacancy formation energy. In contrast, for M=Mn and Zr the O vacancy is preferentially located at the 1NN to M_1 and 3NN to M_2.

For $x=0.09375$ in $Ce_{1-x}M_xO_2$, three dopant ions in the supercell are assumed to be nearest neighbors to each other and an O vacancy is located at the nearest neighbor to all three dopant ions. Figure 12 shows the variation in the O-vacancy formation energies with dopant concentration x in $Ce_{1-x}M_xO_2$. It is seen that each dopant exhibits a characteristic variation in the O-vacancy formation energies with the dopant concentrations. For Zr-doped CeO_2, the formation en-

TABLE I. All the possible defect structures and O-vacancy formation energies in $Ce_{1-x}M_xO_2$ ($x=0.0625$) with M_1, M_2, M=Mn, Pr, Sn, or Zr.

			Vacancy formation energy for M-doped ceria (eV)			
No.	M_1 vacancy	M_2 vacancy	Mn	Pr	Sn	Zr
1	1NN	1NN	−1.18	1.13	1.21	2.26
2	1NN	2NN	−1.12	1.14	1.21	1.86
3	1NN	3NN	−1.25	1.28	1.67	1.76
4	2NN	2NN	−0.68	1.48	2.11	3.06
5	2NN	3NN	−0.41	1.42	2.31	3.09
6	2NN	4NN	−0.42	1.25	2.65	3.03
7	2NN	5NN	−0.58	1.44	2.25	3.00
8	3NN	3NN	−0.59	1.35	2.79	2.95
9	3NN	4NN	−0.09	1.24	2.60	3.02
10	3NN	5NN	0.12	1.38	2.67	3.38
11	3NN	6NN	−0.73	1.56	2.61	2.82
12	3NN	7NN	−0.79	1.36	2.31	3.00
13	4NN	5NN	−0.96	1.35	1.75	2.43
14	4NN	8NN	0.01	1.35	3.04	3.30

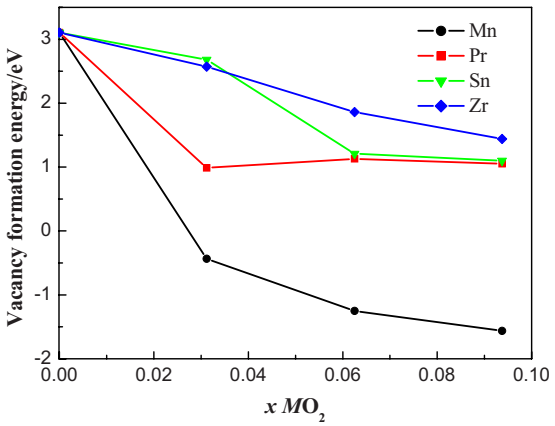

FIG. 12. (Color online) The concentration dependence of the O-vacancy formation energy in $Ce_{1-x}M_xO_2$ with M=Mn, Pr, Sn, and Zr.

ergy decreases gradually with dopant concentrations. For Mn-doped CeO_2, the formation energy decreases strongly at low concentration and then decreases further moderately. Sn-doped CeO_2 exhibits a steplike decrease in the intermediate concentration. Pr dopants decrease the formation energy strongly at low concentration, similarly as Mn, but change the energy hardly upon further doping. The complicated feature in the case of Mn, Pr, and Sn can be ascribed to the effects of the electronic modification as well as the structural distortion with dopant incorporation as discussed in Sec. III B. Almost constant vacancy formation energy for Pr doping may be understood in view of the structural distortions induced by the dopant ions as discussed in Sec. III B. Compared with Mn, Sn, and Zr ion, the radius of Pr^{4+} (0.96 Å) is nearly equal to Ce^{4+}, and the average Pr-O bond length is 2.38 Å which is also close to that of Ce-O bond (2.377 Å). This aspect may make CeO_2 structure rather tolerant of high Pr concentrations.

IV. CONCLUSION

Using the first-principles density-functional theory considering the on-site Coulomb interaction within the PBE $+U$ scheme, we have investigated the effect of the dissolved MnO_2, PrO_2, SnO_2, and ZrO_2 on the atomic structure, electronic structure, and the reduction properties of CeO_2. Results indicate that the O-vacancy formation energies decrease and the reduction are facilitated by doping of all these oxides. Two different mechanisms for the O-vacancy formation in doped CeO_2 have been clarified. Compared with the case of pure CeO_2 the decrease in the O-vacancy formation energy for the Zr-doped CeO_2 is mostly caused by the structural distortion, whereas the decrease for Mn-, Pr-, or Sn-doped CeO_2 originates from the electronic modification as well as from the structural distortion. Therefore the electrons left upon the formation of the O vacancy can localize on the dopant ions instead of host Ce ions. Two effects also contribute to characteristic concentration dependence of the O-vacancy formation energies for different dopants.

ACKNOWLEDGMENTS

The present work is supported by National Natural Science Key Foundation of China (NSFC) (Grant No. 50730004), National Natural Science Foundation of China (NSFC) (Grants No. 50802089 and No. 51072183), Qianjiang Talent Project of Zhejiang Province (Grant No. 2007R10028), and Natural Science Foundation of Zhejiang Province (Grant No. Y4090280). This work is partly supported by WCU (World Class University) program through the Korea Science and Engineering Foundation funded by the Ministry of Education, Science and Technology (Grant No. R32-2009-000-20074-0).

*FAX: 86-571-86843655; siqishihz@gmail.com

[1] M. S. Dresselhaus and I. L. Thomas, Nature (London) **414**, 332 (2001).
[2] F. Esch, S. Fabris, L. Zhou, T. Montini, C. Africh, P. Fornasiero, G. Comelli, and R. Rosei, Science **309**, 752 (2005).
[3] K. Kenevey, F. Valdivieso, and M. Soustelle, Appl. Catal., B **29**, 93 (2001).
[4] Q. Fu, H. Saltsburg, and M. Flytzani-Stephanopoulos, Science **301**, 935 (2003).
[5] G. A. Deluga, J. R. Salge, L. D. Schmidt, and X. E. Verykios, Science **303**, 993 (2004).
[6] S. Park, J. M. Vohs, and R. J. Gorte, Nature (London) **404**, 265 (2000).
[7] B. C. H. Steele and A. Heinzel, Nature (London) **414**, 345 (2001).
[8] T. Hibino, A. Hashimoto, T. Inoue, J.-I. Tokuno, S. I. Yoshida, and M. Sano, Science **288**, 2031 (2000).
[9] B. C. H. Steele, Solid State Ionics **129**, 95 (2000).
[10] M. Mogensen, N. M. Sammes, and G. A. Tompsett, Solid State Ionics **129**, 63 (2000).
[11] S. Babu, R. Thanneeru, T. Inerbaev, R. Day, A. E. Masunov, A. Schulte, and S. Seal, Nanotechnology **20**, 085713 (2009).
[12] X. Liu, K. Zhou, L. Wang, B. Wang, and Y. Li, J. Am. Chem. Soc. **131**, 3140 (2009).
[13] C. Sun, H. Li, H. Zhang, Z. Wang, and L. Chen, Nanotechnology **16**, 1454 (2005).
[14] C. Sun, H. Li, and L. Chen, J. Phys. Chem. Solids **68**, 1785 (2007).
[15] G. Xiao, Z. Jiang, H. Li, C. Xia, and L. Chen, Fuel Cells **9**, 650 (2009).
[16] P. Gao, Z. Kang, W. Fu, W. Wang, X. Bai, and E. Wang, J. Am. Chem. Soc. **132**, 4197 (2010).
[17] N. V. Skorodumova, R. Ahuja, S. I. Simak, I. A. Abrikosov, B. Johansson, and B. I. Lundqvist, Phys. Rev. B **64**, 115108 (2001).
[18] D. A. Andersson, S. I. Simak, B. Johansson, I. A. Abrikosov, and N. V. Skorodumova, Phys. Rev. B **75**, 035109 (2007).
[19] J. L. F. Da Silva, Phys. Rev. B **76**, 193108 (2007).
[20] S. Q. Shi, X. Z. Ke, C. Y. Ouyang, H. Zhang, H. C. Ding, Y. H. Tang, W. W. Zhou, P. J. Li, M. S. Lei, and W. H. Tang, J. Power

Sources **194**, 830 (2009).
[21] S. Q. Shi, Y. H. Tang, C. Y. Ouyang, L. X. Cui, X. G. Xin, P. J. Li, W. W. Zhou, H. Zhang, M. S. Lei, and L. Q. Chen, J. Phys. Chem. Solids **71**, 788 (2010).
[22] D. A. Andersson, S. I. Simak, N. V. Skorodumova, I. A. Abrikosov, and B. Johansson, Phys. Rev. B **76**, 174119 (2007).
[23] D. A. Andersson, S. I. Simak, N. V. Skorodumova, I. A. Abrikosov, and B. Johansson, Appl. Phys. Lett. **90**, 031909 (2007).
[24] M. Nakayama and M. Martin, Phys. Chem. Chem. Phys. **11**, 3241 (2009).
[25] Z. Yang, T. K. Woo, M. Baudin, and K. Hermansson, J. Chem. Phys. **124**, 224704 (2006).
[26] Z. Yang, G. Luo, and Z. Lu, J. Chem. Phys. **127**, 074704 (2007).
[27] B. M. Reddy, P. Bharali, P. Saikia, A. Khan, S. Loridant, M. Muhler, and W. Grulnert, J. Phys. Chem. C **111**, 1878 (2007).
[28] Z. X. Song, W. Liu, H. Nishiguchi, A. Takami, K. Nagaoka, and Y. Takita, Appl. Catal., A **329**, 86 (2007).
[29] T. Y. Zhang, S. P. Wang, Y. Yu, Y. Su, X. Z. Guo, S. R. Wang, S. M. Zhang, and S. H. Wu, Catal. Commun. **9**, 1259 (2008).
[30] Q. Liang, X. Wu, D. Weng, and H. Xu, Catal. Today **139**, 113 (2008).
[31] G. Xiao, S. Li, H. Li, and L. Chen, Microporous Mesoporous Mater. **120**, 426 (2009).
[32] P. E. Blöchl, Phys. Rev. B **50**, 17953 (1994).
[33] G. Kresse and J. Furthmüller, Phys. Rev. B **54**, 11169 (1996).
[34] G. Kresse and D. Joubert, Phys. Rev. B **59**, 1758 (1999).
[35] J. P. Perdew, K. Burke, and M. Ernzerhof, Phys. Rev. Lett. **77**, 3865 (1996).
[36] G. Kresse and J. Furthmüller, Comput. Mater. Sci. **6**, 15 (1996).
[37] G. A. Landrum, R. Dronskowski, R. Niewa, and F. J. DiSalvo, Chem.-Eur. J. **5**, 515 (1999).
[38] M. Nolan, S. C. Parker, and G. W. Watson, Surf. Sci. **595**, 223 (2005).
[39] M. Nolan, S. Grigoleit, D. C. Sayle, S. C. Parker, and G. W. Watson, Surf. Sci. **576**, 217 (2005).
[40] S. Fabris, G. Vicario, G. Balducci, S. de Gironcoli, and S. Baroni, J. Phys. Chem. B **109**, 22860 (2005).
[41] H. J. Monkhorst and J. D. Pack, Phys. Rev. B **13**, 5188 (1976).
[42] M. Methfessel and A. T. Paxton, Phys. Rev. B **40**, 3616 (1989).
[43] P. E. Blöchl, O. Jepsen, and O. K. Andersen, Phys. Rev. B **49**, 16223 (1994).
[44] M. A. Panhans and R. N. Blumwnthal, Solid State Ionics **60**, 279 (1993).
[45] N. V. Skorodumova, S. I. Simak, B. I. Lundqvist, I. A. Abrikosov, and B. Johansson, Phys. Rev. Lett. **89**, 166601 (2002).
[46] Y. Jiang, J. B. Adams, and M. V. Schilfgaarde, Appl. Phys. Lett. **87**, 141917 (2005).
[47] D. A. Andersson, S. I. Simak, N. V. Skorodumova, I. A. Abrikosov, and B. Johansson, Proc. Natl. Acad. Sci. U.S.A. **103**, 3518 (2006).
[48] E. Wuilloud, B. Delley, W. D. Schneider, and Y. Baer, Phys. Rev. Lett. **53**, 202 (1984).
[49] S. Fabris, S. de Gironcoli, S. Baroni, G. Vicario, and G. Balducci, Phys. Rev. B **71**, 041102 (2005).
[50] J. L. F. Da Silva, M. V. Ganduglia-Pirovano, J. Sauer, V. Bayer, and G. Kresse, Phys. Rev. B **75**, 045121 (2007).
[51] W. Shan, N. Ma, J. Yang, X. Dong, C. Liu, and L. Wei, J. Nat. Gas Chem. **19**, 86 (2010).
[52] C. Y. Kang, H. Kusaba, H. Yahiro, K. Sasaki, and Y. Teraoka, Solid State Ionics **177**, 1799 (2006).
[53] M. V. Ganduglia-Pirovano, J. L. F. Da Silva, and J. Sauer, Phys. Rev. Lett. **102**, 026101 (2009).
[54] H. Li, H. Wang, X. Gong, Y. Guo, Y. Guo, G. Lu, and P. Hu, Phys. Rev. B **79**, 193401 (2009).
[55] A. Bianconi, A. Kotani, K. Okada, R. Giorgi, A. Gargano, A. Marcelli, and T. Miyahara, Phys. Rev. B **38**, 3433 (1988).
[56] H. Ogasawara, A. Kotani, K. Okada, and B. T. Thole, Phys. Rev. B **43**, 854 (1991).
[57] S. M. Butorin, L. C. Duda, J. H. Guo, N. Wassdahl, J. Nordgren, M. Nakazawa, and A. Kotani, J. Phys.: Condens. Matter **9**, 8155 (1997).
[58] F. Tran, J. Schweifer, P. Blaha, and K. Schwarz, Phys. Rev. B **77**, 085123 (2008).
[59] G. Balducci, J. Kaspar, P. Fornasiero, M. Graziani, and M. S. Islam, J. Phys. Chem. B **102**, 557 (1998).
[60] Y. C. Chen, K. Chen, C. Lee, and M. C. Lin, J. Phys. Chem. C **113**, 5031 (2009).
[61] G. Dutta, U. V. Waghmare, T. Baidya, M. S. Hegde, K. R. Priolkar, and P. R. Sarodec, Catal. Lett. **108**, 165 (2006).
[62] J. A. Rodriguez, J. C. Hanson, J. Y. Kim, G. Liu, A. Iglesias-Juez, and M. Fernandez-Garcia, J. Phys. Chem. B **107**, 3535 (2003).
[63] A. D. Mayernick and M. J. Janik, J. Phys. Chem. C **112**, 14955 (2008).
[64] M. Yashima, J. Phys. Chem. C **113**, 12658 (2009).
[65] M. Nolan, J. Phys. Chem. C **113**, 2425 (2009).
[66] G. Zhou and R. J. Gorte, J. Phys. Chem. B **112**, 9869 (2008).
[67] X. Wang, J. C. Hanson, G. Liu, and J. A. Rodriguez, J. Chem. Phys. **121**, 5434 (2004).